13th International Symposium on Particle Image Velocimetry – ISPIV 2019
Munich, Germany, July 22-24, 2019

High-speed PIV at the exit of a lean-burn combustion chamber operated at elevated pressure

Christian Willert[1*], Michael Schroll[1], Johannes Heinze[1], Thomas Soworka[1]

[1] German Aerospace Center (DLR), Institute of Propulsion Technology, Köln, Germany

[*] chris.willert@dlr.de

Abstract

High-speed particle image velocimetry measurements were performed at the exit of a pressurized lean-burn combustion chamber fueled with kerosene and operated at flight relevant conditions (elevated pressure and pre-heated supply air). The aim was to obtain information on the turbulent nature of the exhaust flow as this is of relevance for the modelling of aero-thermal dynamics of the combustor-turbine interface, such as heat transfer on the outlet guide vanes and turbulence induced noise. Two-component velocity data was sampled at 20 kHz along a narrow strip and used to obtain frequency spectra and correlations. Synchronously acquired chemiluminescence of the OH radical in the primary zone exhibited a notable tonal peak near 100 Hz that could also be detected in the circumferential velocity component at one operating condition.

1 Introduction

In order to meet ACARE's "Flightpath 2050" requirements, next generation aero-engines need to be significantly optimized with regard to fuel-efficiency and reduced pollutant and noise emissions. On the combustor side, the highest potential of meeting these stringent goals is by implementing lean burn technologies. However, compared to conventional combustion technology, lean burn combustion has a tendency to be noisier such that the reduction of noise in itself becomes a substantial challenge. In this context the experimental and numerical investigation of combustor induced engine noise was the main subject within the EU Horizon2020 funded CleanSky2 Project "CORNET" (CORe Noise Engine Technology). To validate the employed numerical approaches, the experimental effort within the project was to provide reference data from experimental configurations operating at realistic, ideally flight-relevant, operating conditions of the propulsion system (Langella et al., 2019). To fulfil this purpose, DLR operates several single and multi-sector pressurized combustion rigs that feature good optical access to the combustion environment (Meier et al., 2015; Hassa et al., 2017). A first set of measurements provided the time-varying temperature along a profile in the exit of a combustion chamber using thermometry based on high-speed laser-induced fluorescence (LIF) of the hydroxyl radical (manuscript in preparation). Subject of the present contribution, is a second set of measurements that provided time-varying velocity profiles at the combustor exit, which, combined with the temperature measurements, provide valuable information on the spatio-temporal nature of the flow exiting the combustion chamber and entering the turbine. To the best of the authors' knowledge, temporally resolved multi-point data of both temperature and velocity of a realistic combustor configuration operated at flight relevant conditions so far have not been available.

2 Experimental methods

2.1 Combustion test facility

Time resolved velocity profiles were acquired at the exit of a combustion chamber containing a swirled, lean-burn fuel injector. Details on the pressurized combustion chamber design, shown in Fig. 1, and associated test facility can be found in (Schroll et al., 2017; Hassa et al., 2018; DLR Institute of Propulsion Technology, 2015). The combustor liner, shown in Fig. 1, left, closely simulates the combustion chamber of

an actual aero-engine. The schematic indicates three zones with (A) indicating the primary zone of combustion downstream of the fuel injector, followed by a recirculation and mixing zone (B) before the flow exits the combustion chamber at (C). The lean burn fuel injector consists of a concentric arrangement of a main (outer) fuel stage embedded into large swirling air streams. The large swirling air streams carry the largest portion of the combustor air. A nested pilot (inner) fuel injector is located on the central axis of the injector. Both the pilot and the main module rely on pre-filming airblast fuel injection.

For the measurements presented herein the facility is operated at an elevated pressure ($P_{30} > 10$ bar) at two test conditions (TP) which mainly differ in terms of fuel staging. For TP1 the fuel loading of the main (outer) stage is higher whereas at TP2 the fuel split on the fuel injector is roughly balanced between the main (outer) and pilot (inner) stage. The air-fuel ratio (AFR) for TP1 is about 30% lower compared to TP2. Preheating (T_{30}) of the air entering the combustion chamber is kept constant for both TP.

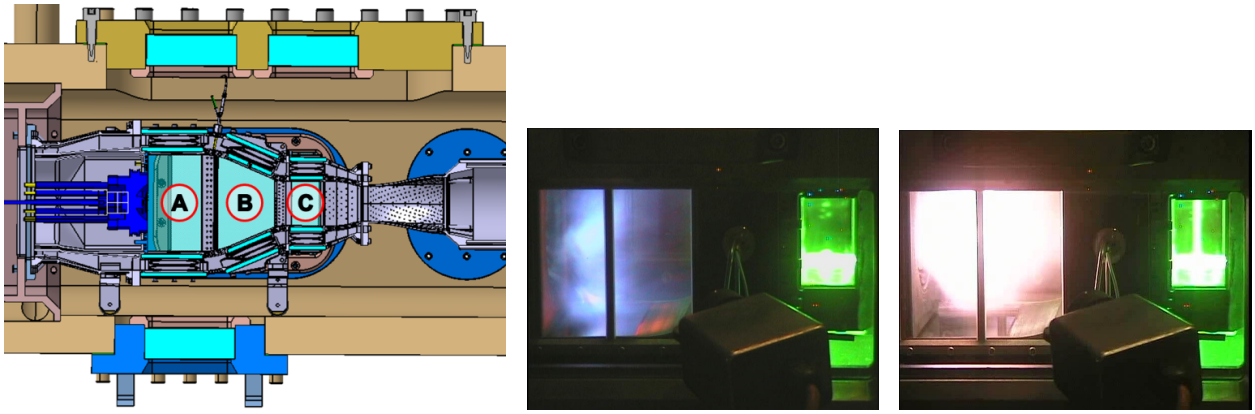

Figure 1: CAD drawing of combustor liner (left) inside the pressure vessel indication different zones within the combustion chamber; right: photographs of combustion rig operating in at TP1 (middle) and TP2 (right) at flight relevant pressure. Visible on the right is the green beam of the high-speed laser illuminating the exit duct.

2.2 Optical diagnostics

The employed high-speed "profile PIV" technique, described by Willert (2015), relies on capturing a narrow image strip of the flow under investigation with the advantage of achieving higher framing rates while at the same time allowing the use of lasers of reduced power in comparison to what would be needed for conventional large area illumination. Based on experiences gained with previous applications of PIV in combustion, the flow inside the plenum upstream of the fuel injector was seeded with micron-sized porous silica micro-spheres (1-2 μm mean dia., Schroll et al., 2017). The seed powder was dispersed using a fluidized bed seeding device (Willert and Jarius, 2002), that could be remotely switched from bypass to seeding mode in order to prevent unnecessary contamination of the facility windows between the short duration PIV data acquisition periods.

The area of interest was illuminated by a pair of pulsed, solid state diode lasers (Innolas Photonics, nanio-Air) with a combined average power of 20W at a wavelength of 532 nm. Their combined beams were focussed to a light sheet of about 6 mm width and 0.3 mm thickness at the waist. The lasers were each operated at 20 kHz and provided double-pulses ($\Delta t = 4\,\mu$s) synchronized to a high speed camera (iX-Cameras, iSpeed726) capturing images at 40 000 frames/s. The high-speed CMOS camera (iX-Cameras, iSpeed 726) features a sensor array of 2048×1536 ($W \times H$) square pixels at a pitch of 13.5 μm and a maximum sample rate of 26 GPixel/s or 8500 frames/s at full resolution. By reducing the field of view, the frame rate can be increased nearly proportionally such that in excess of 40 000 frames/s are possible when imaging a narrow strip of $2048W \times 132H$ pixels. Using a macro lens (Nikon, Mikro-Nikkor f=200 mm, f/4) the image magnification was set at $m = 0.45$ and $m = 0.61$ for two light sheet arrangements, thereby capturing respective areas of interest of about $3 \times 45\,\text{mm}^2$ and $4 \times 60\,\text{mm}^2$ in the rectangular exit duct of the combustion chamber. Remote focusing capability allowed the lens to be refocused during facility operation.

For the HS-PIV measurements the camera was operated in burst mode, acquiring a predefined number of images upon external triggering at 1 Hz intervals. For this mode of operation the camera's memory of 96GB was partitioned to acquire a total of 4 burst sequences of 24 GB each, consisting of up to 62 000

images at 12 bit/pixel. For each of the two operating conditions two independent burst sequences could be acquired after which the data had to be downloaded from the camera, a process requiring about 2 hours. The excessive download time limited the number of recordings that could be acquired during a single rig operating day.

As outlined in Fig. 2, left, the light sheet was introduced in two configurations. Configuration LS1 images a radial profile (along the Z-axis) while LS2 provides a circumferential profile (along the Y-axis) at a fixed radial position.

To correlate the velocity measurements at the combustor exit with the heat release in the primary zone (A), the time series of the integral OH* chemiluminescence signal was acquired using a high-speed photomultiplier. For this purpose, the broadband combustion luminescence was spectrally filtered by a narrowband interference filter (LC 315 ± 10 nm) to single out the OH* chemiluminescence. This signal was then imaged by an achromatic UV lens (Nikon, Nikkor UV f=105 mm, f/4.5) onto a rectangular aperture to define the region of interest (ROI) as outlined in Fig. 2, right. The integral OH* across the ROI was detected by a photomultiplier (PM Hamamatsu 1P28) combined with a fast preamplifier (Hamamatsu C7319) that was set at a cut-off frequency of 20 kHz. During the measurements it was found that a reduction of the area of interest to only collect chemiluminescence from the upper half of the primary zone produced distinct tonal components in the frequency spectra (Fig. 3). This is believed to be caused by a cyclic behavior of the flame in the primary zone, possibly induced by a precessing vortex structure downstream of the fuel injector. Fig. 3 illustrates the effect of the area-selective OH-chemiluminescence recording for two test points, with one exhibiting a distinct tonal component only when the field of view is reduced to collect only the signal from the upper half of the primary zone.

The entire optical instrumentation was mounted onto a large, three-axis translation table that allowed the imaging systems to be moved in unison without the need of intermediate realignment of the camera with respect to the light sheet.

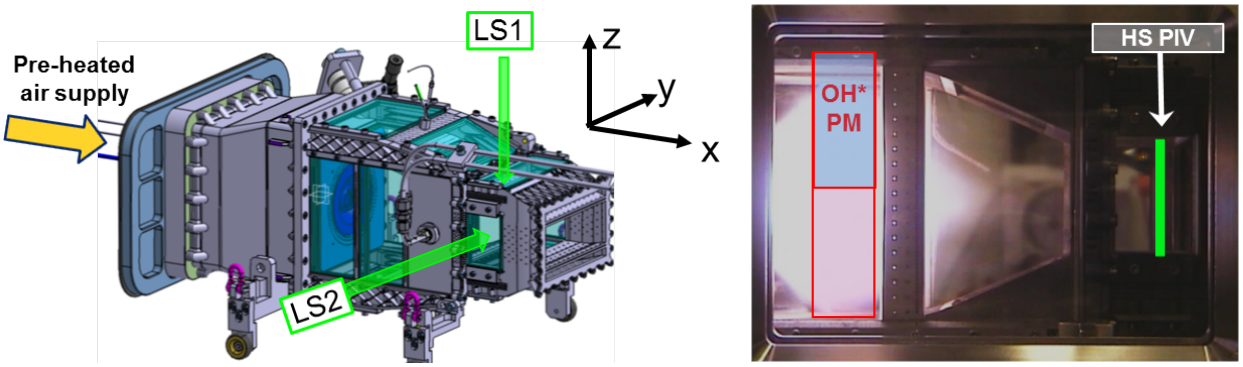

Figure 2: Left: CAD drawing of combustor liner showing orientation of the PIV light sheets and coordinate system; right: photograph of operating combustion rig indicating the area of data collection.

2.3 Particle imaging issues

Aside from providing adequate seeding to a pressurized, reacting environment, the image quality is affected by density gradients along the optical path between source (particle) and collecting lens (camera lens). The density gradients lead to a combination of deflection of the optical path and a blurring of the imaged object. The effects can be reduced by closing the lens aperture (i.e. limiting the collection angle) or by increasing the working distance. The limited laser power excluded a reduction of the lens aperture whereas an increased working distance would have required an objective lens with a higher focal length resulting in a corresponding reduction of the aperture (light gathering capability).

Initial trial measurements performed near the middle plane ($y = 0$) exhibited significant amounts of image blurring with particle images reaching sizes in excess of 20 pixels. An example is shown in the top sub-figure of Fig. 4 where the top sub-figure represents data acquired near the center of the duct. Strongly blurred particle images can be observed near the left edge ($z \approx 16$ mm) whereas other parts are less affected. Overall the particle images are significantly above the optimum (e^{-2}) diameter of 2-3 pixels. Due to the blurring the effective particle image density is reduced as weaker particles cannot be detected over the background noise of the imaging sensor. Images acquired closer toward the side wall of the duct (Fig. 4,

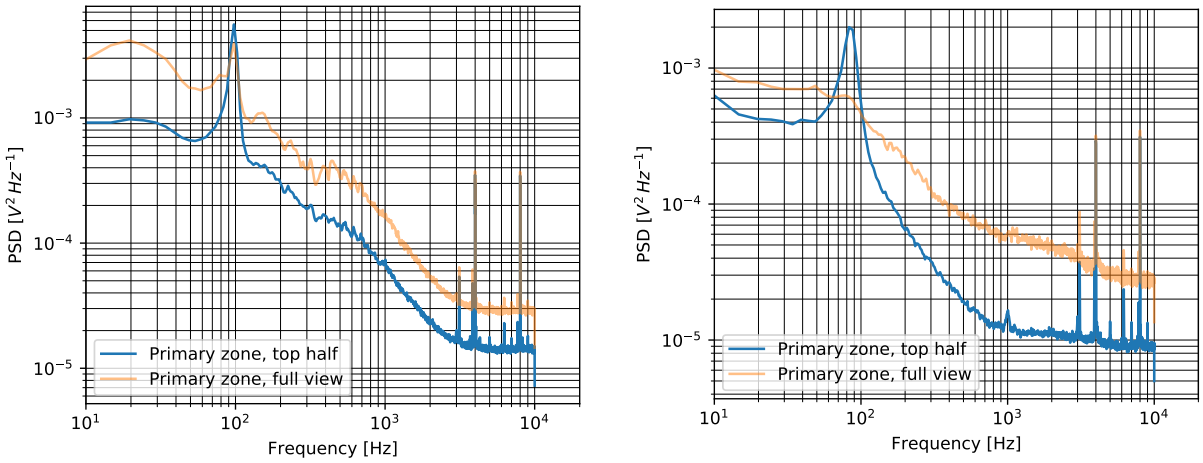

Figure 3: Spectra of the OH*-chemiluminescence signal acquired in the primary zone with different regions of interest for two test conditions. The orange lines represent spectra of the OH* acquired across the entire primary zone, whereas the blue lines represent signals collected from the upper portion only.

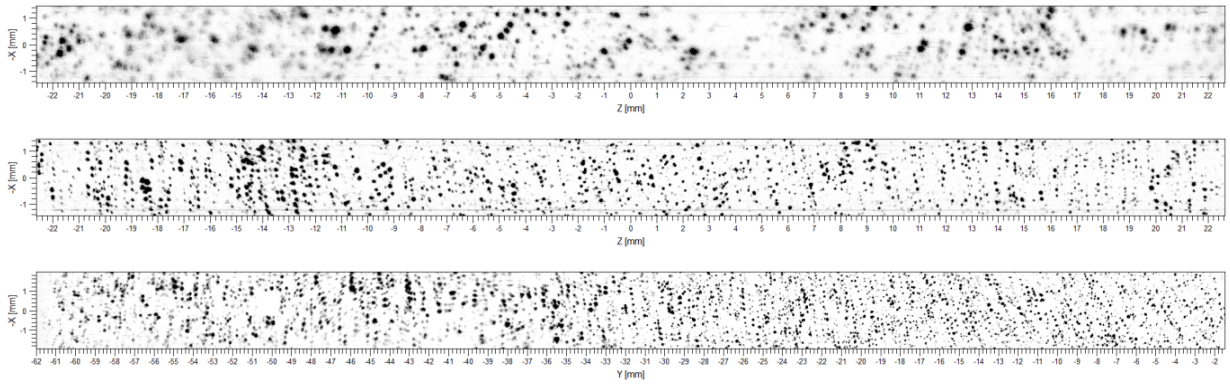

Figure 4: Exemplary PIV images obtained near the combustor center, $y/W = 0$ (top), for configuration LS1 at $y/W = -0.33$ (middle) and at $z/H = +0.33$ for configuration LS2 (bottom, LS2). For visual reasons, image intensity is inverted showing bright particles as black spots.

middle) exhibit an overall much improved particle diameter range along with a reduction of blurring. The reduction of the magnification factor for light sheet configuration LS2 further improves the image quality in accordance to the reduction of effective spatial resolution (Fig. 4, bottom). Here, the mean particle image diameter varies between 3 and 5 pixels. Nonetheless, image blurring due to density gradients can be observed in the left portion of the image in the form of locally increased particle image diameters. A shot-to-shot variation of the image blurring, due to continually changing changes in refractive index along the optical path was also observed but is not further characterized herein.

2.4 Data processing

Multiple image sequences, each consisting of short bursts between 3100 and 4400 image pairs triggered at 1 Hz intervals, were captured at 20 kHz for the two operating conditions with varied fuel staging and otherwise fixed preheating and plenum pressure. The acquired image data was then processed with an established 2D-2C, coarse-to-fine cross-correlation PIV algorithm using samples of 32×32 pixels or 48×48 pixels a the final evaluation stage. From the processed gridded 2-C velocity data the central column of data was extracted and compiled into velocity-vs-time records for which representative samples are shown in Fig. 5. These time-evolving velocity profiles constitute the basis for further data post-processing to retrieve

relevant statistics, frequency spectra, correlations and other quantities presented in the following section. The validation rates are on the order of 99 percent based for the bulk of the data, decreasing to 95 percent near the edges of the imaged area. Validation relied normalized median validation scheme (Westerweel and Scarano, 2005) with a threshold level set at 3.0 and a Chauvenet cut-off at 5 standard deviations from the mean.

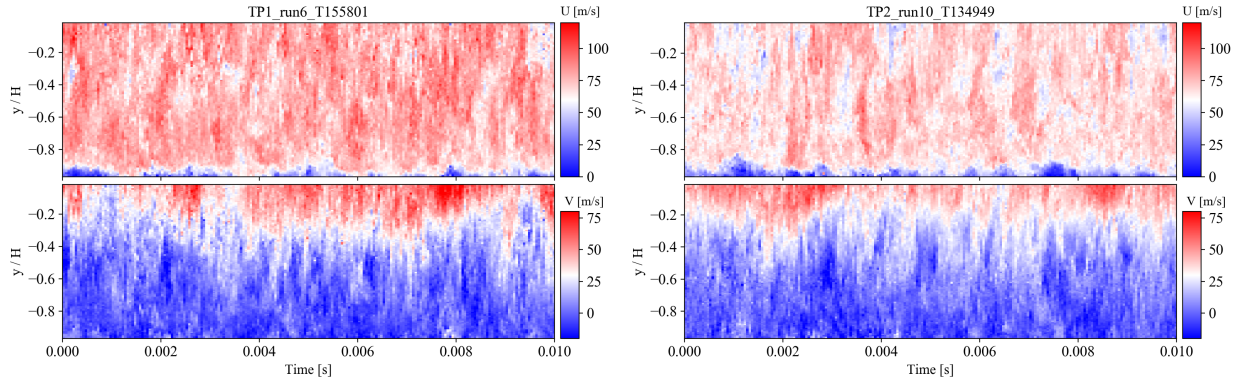

Figure 5: Subset of 200 samples (0.010 s) of the time-evolving velocity profiles for component U (top) and V (bottom) at the combustor exit for two fuel staging conditions of imaging configuration LS2.

3 Results

Given the velocity-vs-time records, of which a short segment is shown in Fig. 5, profiles of the mean and variances can be readily computed. The velocity profiles, shown in Fig. 6, are nearly self-similar between the two test points, with the mean velocity about 20% higher for TP1, in agreement with velocity data acquired by conventional PIV (see e.g. Fig.5 in Schroll et al., 2017). For imaging configuration LS2, the streamwise velocity U exhibits a block-shaped mean profile with a boundary layer visible near the wall ($y/W < 0.45$). The increasing circumferential velocity V toward the center of the duct $y/W = 0$ is associated with the large scale swirl introduced by the fuel injector. The absolute velocity fluctuations in LS2 also vary uniformly with the change in test point, peaking toward the center of the duct and the center of the swirl. For LS1 the fluctuations also peak in the center at $z/H = 0$. Except for the boundary layer region at $y/W < 0.45$, the Reynolds stress, $\langle u'w' \rangle$ for LS1 and $\langle u'v' \rangle$ for LS2, is essentially zero for the bulk of the flow.

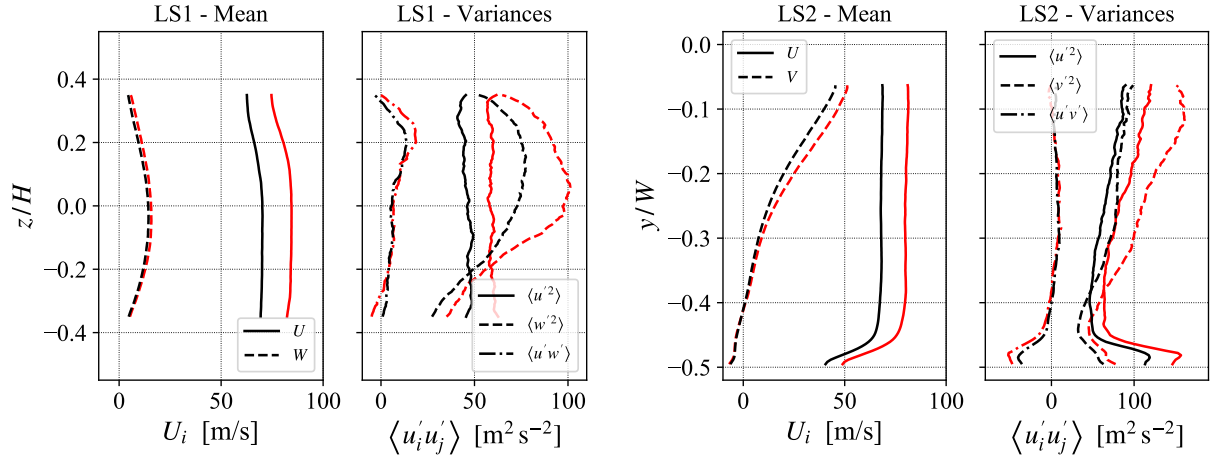

Figure 6: Profiles of mean velocity and variances obtained at the combustor exit for imaging configuration LS1 (left) and LS2 (right). Red lines were obtained for TP1, black lines for TP2.

Probability density functions (PDF) for the respective velocity components are presented in Fig. 7. With the probability plotted on a logarithmic scale, the near parabolic shape of the profiles indicate a Gaussian distribution of the fluctuating velocity around the mean. The PDFs also indicate that, in spite of the image sensor's rather large pixel size of 13.5 μm, the recovered velocity data is essentially free of pixel locking, a bias of the displacement data toward integral pixel values and known to result from undersampled particle image data (e.g. particle images with a e^{-2} diameter less of than 2 pixel). In part, this is attributed to density gradient induced blurring of the particle images, as described in the previous section. Given the rather high dynamic range of displacements covering 10 or more pixels, the influence on the velocity statistics and spectra is known to be of lesser significance (Christensen, 2004; Foucaut et al., 2004). A slight amount of pixel locking can be noticed for configuration LS2, which is a result of overall smaller particle images associated with the decreased magnification of LS2 (e.g. $\approx 25\%$ larger field of view).

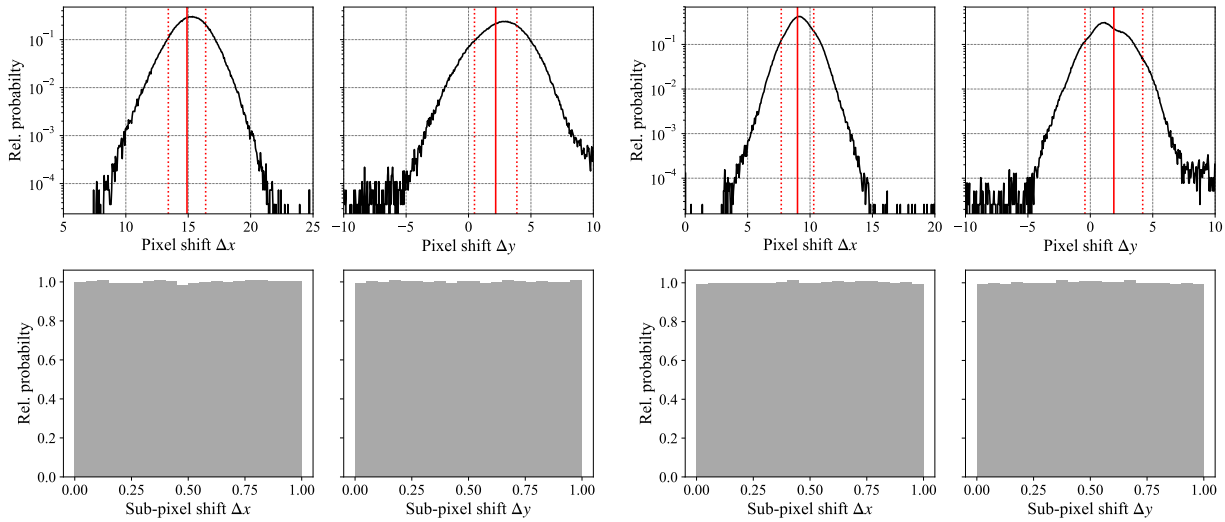

Figure 7: Probability density functions of the velocity components for light sheet configuration LS1 (left) and LS2 (right). Data is sampled in the ranges $-0.4 < y/W < -0.15$ and $z/H < \pm 0.2$. Red solid lines indicate mean values, dotted line one standard deviation from the mean. Lower row of sub-figures represent fractional parts of the pixel displacement after subtracting the integer value.

Frequency spectra are computed by averaging periodograms (Welch, 1967) of the velocity time records at a given spatial location along the profile. Shown in Fig. 8, TP2 shows no notable spectral features on either of the velocity components, whereas the circumferential component V exhibits a pronounced peak near 100 Hz that was also observed in the OH* chemiluminescence data (see Fig. 3). This fluctuation is likely related to periodic flow structures induced by the fuel injector, such as precessing vortex cores commonly observed in the flow field downstream of swirled fuel injectors. The spectra are limited by the Nyquist frequency $f_{\mathrm{PIV}}/2 = 10\,\mathrm{kHz}$ and show no typical roll-up due to PIV related spatial sampling of velocity information. An increased PIV sampling rate in the range of 50 kHz would have been more adequate to resolve the higher frequency content.

While the spectra provided in Fig. 8 represent the frequency distribution at one position along the velocity profiles, the spatially resolved data can be used to for the calculation of spatially resolved frequency spectra such as presented in Fig. 9. This representation clearly highlights the areas with high tonal content such as a pronounced frequency peak of the transverse velocity V at TP1 near the duct's centerline where the velocity fluctuations also reach their maximum. TP2, on the other hand, exhibits a much broader spectral distribution for V that also peaks toward the centerline. For the streamwise velocity U spectral peaks can only be observed in the duct's boundary layer at $y/W < 0.45$.

The time resolved velocity data further allows the calculation of the integral time scales Λ_{u_i} for the respective velocity components through the integration of the associated autocorrelation functions R_{u_i,u_i} (Pope, 2000):

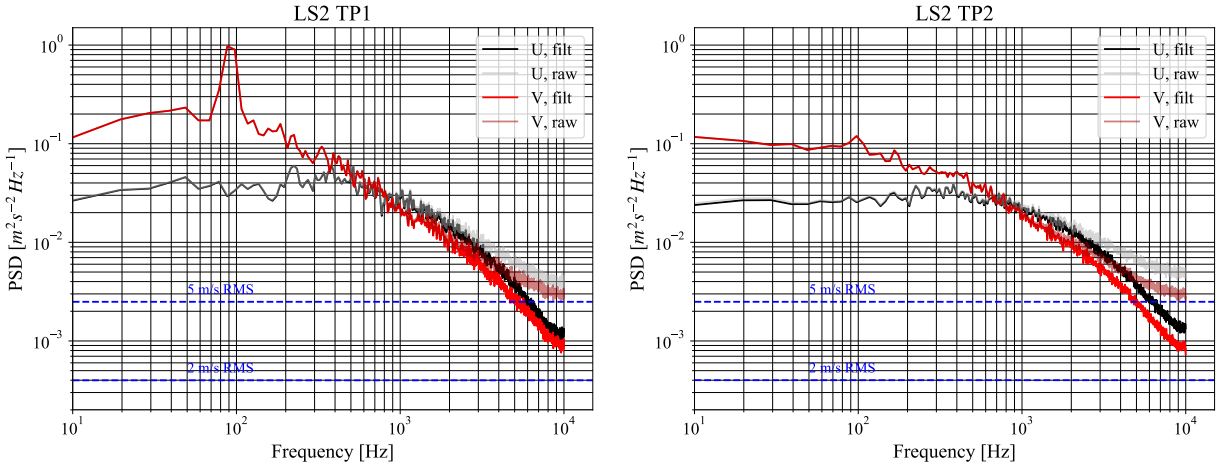

Figure 8: Frequency spectra at the combustor exit for two fuel staging conditions obtained for LS1 at $y/H = -0.2$. The dashed blue lines indicate discrete white noise levels.

$$\Lambda_{u_i} = \int_{t=0}^{\infty} R_{u_i,u_i}(\tau)\mathrm{d}t \quad (1)$$

$$R_{u_i,u_i}(\tau) = \int_{-\infty}^{\infty} u_i(t)u_i(t+\tau)\mathrm{d}t \quad (2)$$

This calculation is performed at each spatial sampling location, such that profiles of the estimated integral time scales are obtained. Shown in Fig. 10, it is evident that the time-scales vary strongly across the cross-section of the exit duct, with the fuel-split variation having only a minor influence. More significant is the strong anisotropy of up to a factor of 4 between the axial and circumferential integral time scales, most likely due to acceleration effects in the convergent zone immediately upstream of the exit duct. Near the combustor liner the streamwise timescales increase due to the presence of the wall-boundary layer and effusion cooling flows.

Finally, Fig. 11 demonstrates the value of simultaneous correlated measurements of different quantities. It shows spatially resolved maps of the correlation between the radial velocity component and the integral OH* chemiluminescence captured in the primary zone. The shape of the correlation contours give an indication of the phase shift between the two signals. Whereas the chemiluminescence does exhibit a significant tonal component near 100 Hz for all operating points (cf. Fig. 3), it can only be observed in the velocity data for one operating point (Fig. 8, left). Consequently, the correlation map for TP2 is essentially zero indicating that the flow leaving the combustor is essentially free of notable modulation.

4 Conclusion

The material presented herein demonstrates the feasibility of applying high-speed PIV in the rough operating environment of a kerosene fueled combustion chamber operating at flight relevant conditions. The time-resolved data acquired in the exit duct allows the estimation of velocity spectra, two-point correlations and turbulent time scales that are important for the improved modelling of the aero-thermal processes at the combustor turbine interface. For test points exhibiting a strong periodicity in the heat release, a notable modulation could also be observed in the velocity, in particular, for the circumferential component representing the swirling motion originally introduced by the fuel injector itself. In combination with other high-speed diagnostics such as OH* chemiluminescence imaging presented here or sound pressure monitoring, correlations between the measurands can provide further insight into the dynamics of the reacting combustor flow.

From the experimental point of view, the overall data quality will benefit from a few modifications. For the present measurements, both the sampling rate and the number of acquired records were limited by the

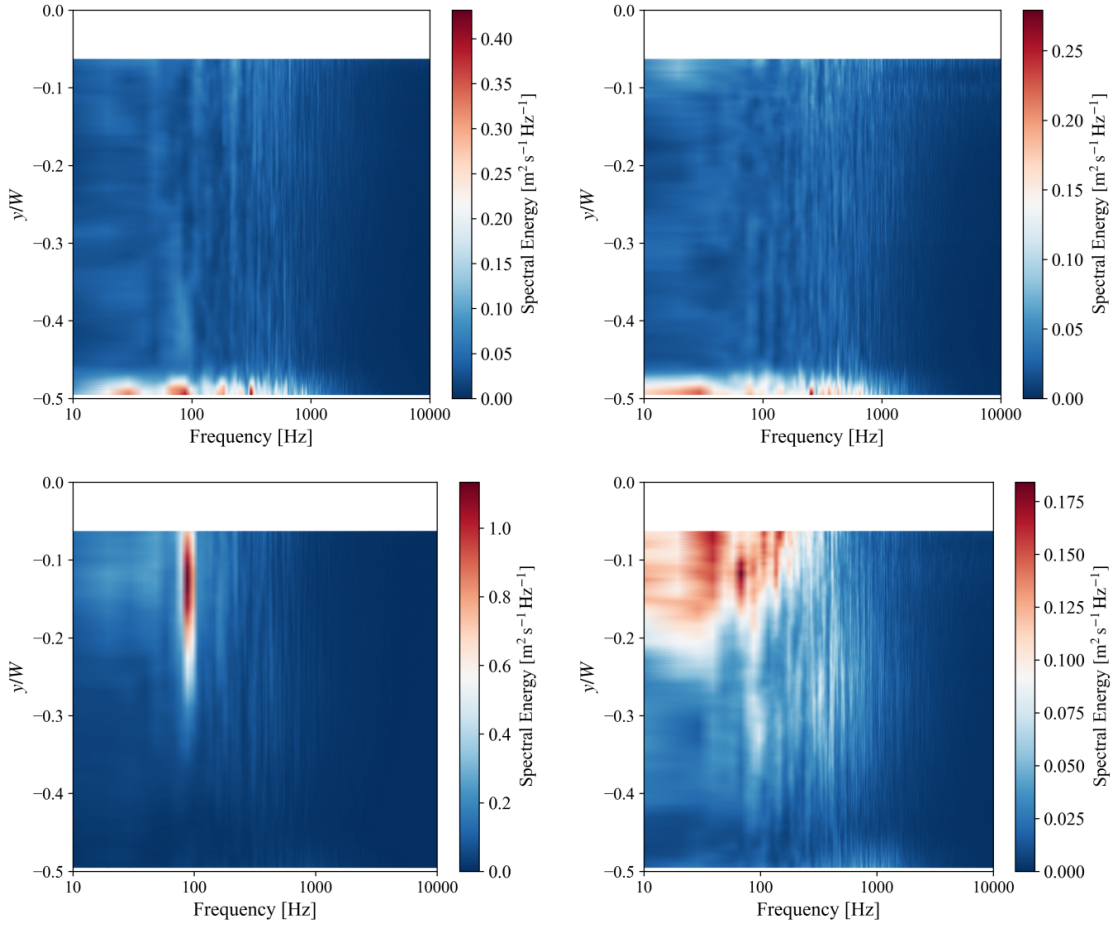

Figure 9: Spatially resolved frequency spectra of velocity components U (top) and V (bottom) for TP1 (left column) and TP2 (right column) obtained from imaging configuration LS2.

available laser power and the amount of memory installed in the high-speed camera. This limited the degree of convergence of retrieved statistics, correlations and spectra. It is clear, that fast camera download rates are essential to increase the overall data yield. Furthermore, the image data could not be evaluated with sample sizes smaller than $1 \times 1\,\mathrm{mm}^2$ (32×32 pixel) which is due to insufficient particulate seeding. The increased magnification of the described imaging setup requires a proportional increase of seeding in comparison to the previously applied macroscopic PIV for which the seeding amount was optimized. Given the short measurement times of high-speed PIV of typically a few tens of seconds and, along with it, comparatively short seeding durations, the additional seeding will have little impact on increased window contamination. In the present seeding configuration, conventional PIV measurements can be performed over several hours without significant build-up of seeding deposits on the windows (Schroll et al., 2017).

The high-speed PIV measurements presented herein further demonstrated that variations in the refractive index results in image blurring which in turn offsets issues commonly associated with large sensor pixels of high-speed cameras, such as pixel locking. Nonetheless, this image blurring can become so severe such that suitable PIV recordings can no longer be acquired. One known solution to this issue is the reduction of the lens aperture which, however, requires a proportional increase in laser power to obtain similar image intensity levels. In this regard, the light sensitivity of current generation high-speed CMOS cameras have improved considerably in comparison to those available a decade ago.

Acknowledgements

The authors acknowledge funding from the Clean Sky 2 Joint Undertaking under the European Union's Horizon 2020 research and innovation programme (grant agreement No 686332) which made these measurements possible.

References

Christensen KT (2004) The influence of peak-locking errors on turbulence statistics computed from PIV ensembles. *Exp Fluids* 36:484–497

DLR Institute of Propulsion Technology (2015) High pressure combustion test facility HBK1. `http://www.dlr.de/at/desktopdefault.aspx/tabid-1509/2443_read-3809/`. accessed: 2019-04-30

Foucaut JM, Carlier J, and Stanislas M (2004) PIV optimization for the study of turbulent flow using spectral analysis. *Meas Sci Technol* 15:1046–1058

Hassa C, Meier U, Heinze J, Schroll M, Magens E, and Bagchi I (2017) Investigation of the reacting flow field of a lean burn injector with varying degree of swirl at elevated pressure condition. in *Proceedings of ASME Turbo Expo 2017: Turbomachinery Technical Conference and Exposition GT2017, June 26-30, 2017, Charlotte, NC, USA*

Hassa C, Voigt L, Schroll M, Heinze J, Willert C, and Bagchi I (2018) Optische Messung von Geschwindigkeit und Temperatur am Austritt einer Magerbrennkammer unter realistischen Betriebsbedingungen. in *Deutsche Gesellschaft für Luft- und Raumfahrt - Lilienthal-Oberth e.V.*

Langella I, Swaminathan N, Zedda M, Heinze J, and Voigt L (2019) Turbulent flame shape switching at conditions relevant for gas turbines. in *Proceedings of ASME. Turbo Expo: Power for Land, Sea, and Air; Phoenix, Arizona, USA, 17-21 June 2019*. pages GT2019–91879

Meier U, Heinze J, Magens E, Schroll M, Hassa C, Bake S, and Doerr T (2015) Optically accessible multisector combustor: Application and challenges of laser techniques at realistic operating conditions. in *Proceedings of ASME. Turbo Expo: Power for Land, Sea, and Air, Volume 6; Montreal, Quebec, Canada, 15–19 June 2015*

Pope SB (2000) *Turbulent Flows*. Cambridge Univ. Press, Cambridge, UK

Schroll M, Doll U, Stockhausen G, Meier U, Willert C, Hassa C, and Bagchi IK (2017) Flow field characterization at the outlet of a lean burn single sector combustor by laser-optical methods. *Journal of Engineering for Gas Turbines and Power* 139:011503–011503

Welch P (1967) The use of fast Fourier transform for the estimation of power spectra: A method based on time averaging over short, modified periodograms. *IEEE Transactions on Audio and Electroacoustics* 15:70–73

Westerweel J and Scarano F (2005) Universal outlier detection for PIV data. *Experiments in Fluids* 39:1096–1100

Willert C and Jarius M (2002) Planar flow field measurements in atmospheric and pressurized combustion chambers. *Experiments in Fluids* 33:931–939

Willert CE (2015) High-speed particle image velocimetry for the efficient measurement of turbulence statistics. *Experiments in Fluids* 56:17

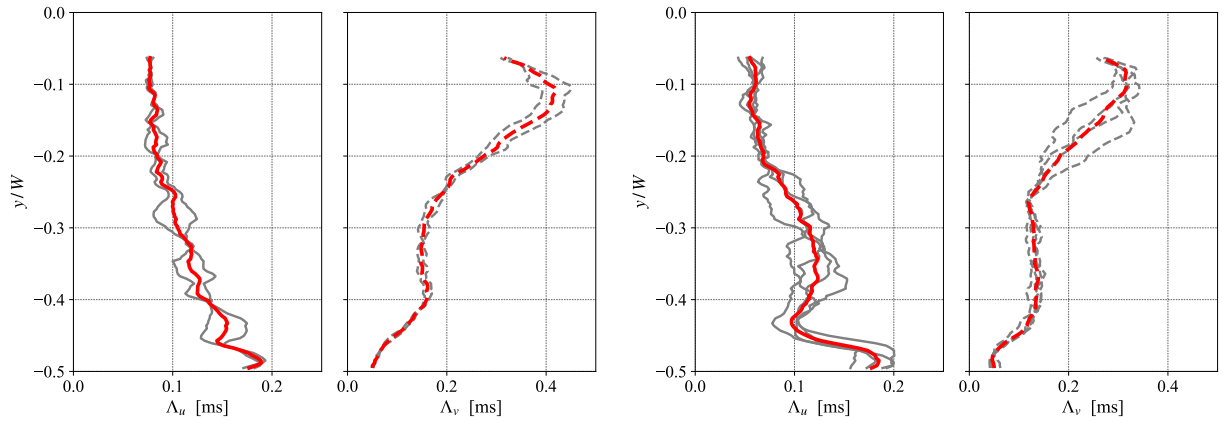

Figure 10: Integral time scale estimates at LS2 calculated through integration of autocorrelation of the velocity components for TP1 (left) and TP2 (right). Solid lines represent time scales associated with axial velocity U, dashed lines are associated with circumferential velocity V.

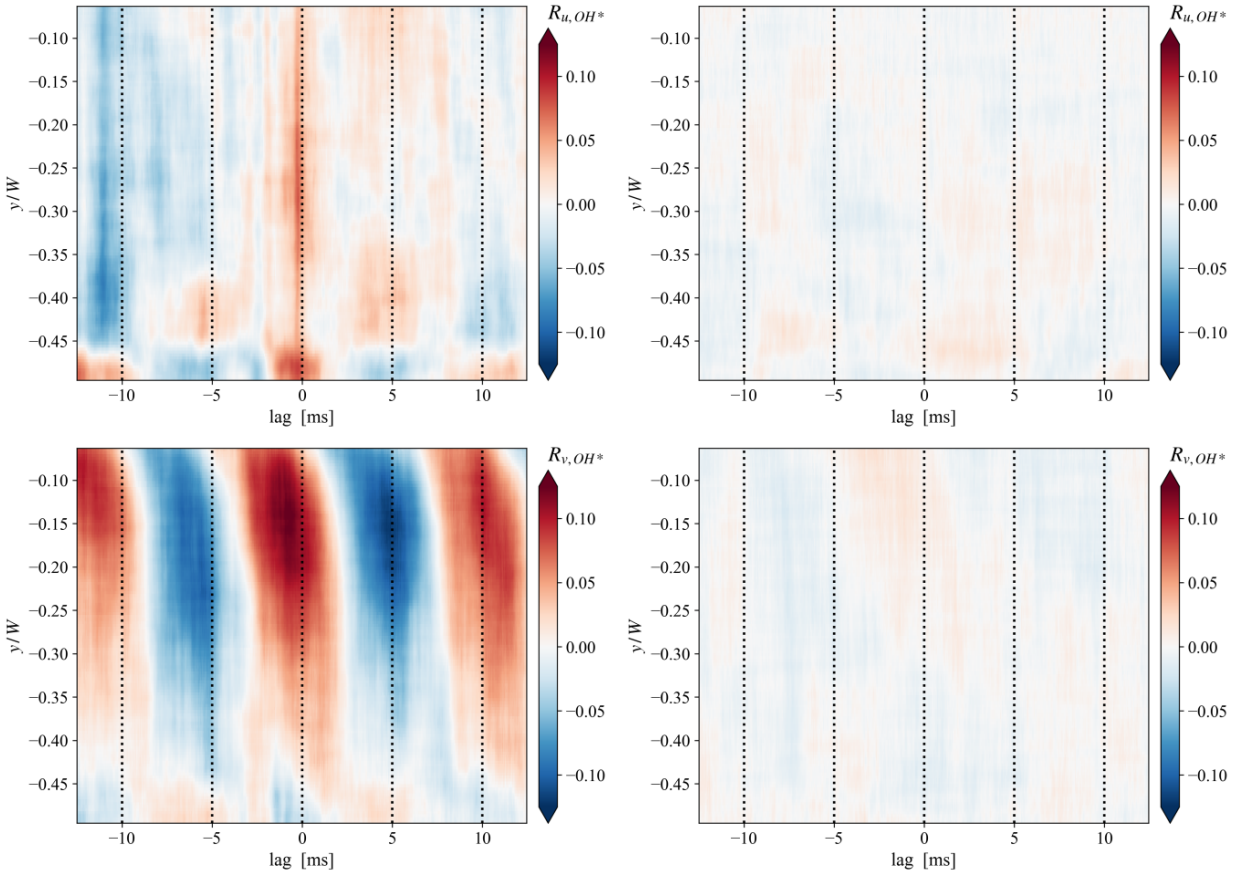

Figure 11: Spatially resolved cross-correlation between OH* chemiluminescence of the primary zone and the measured velocity components in exit duct for TP1 (left) and TP2 (right) obtained from imaging configuration LS2.